submitted to Geophys. J. Int.

3-D Crustal Shear Wave Velocity Model Derived from the Adjoint Waveform Tomography in the Central Japan Island

Kota Mukumoto[1], Takeshi Tsuji[1,2]

[1] Department of Earth Resources Engineering, Kyushu University, Fukuoka, Japan

[2] International Institute for Carbon-Neutral Energy Research (I2CNER), Kyushu University, Fukuoka,Japan

26 August 2021

SUMMARY

Adjoint waveform tomography, which is an emerging seismic imaging method for the crust- and global-scale problems, has gained popularity in the past and present decade. This study, for first time, applies adjoint waveform tomography to the large volume of seismic data recorded by the densely spaced, permanent monitoring network that covers the entirety of Japan. We develop a heterogeneous shear-wave velocity model of central Japan that agrees with the geology and lithology. The results reduce the time-frequency phase misfit by 18.0% in the 0.033–0.1 Hz frequency band and 1.6% in the 0.033–0.125 Hz band, respectively. We infer that some velocity anomalies resolved in this work reflect the volcanic fluids, thick sedimentary basins, and granitic rocks. The results of this study suggest the possibility of imaging heterogeneous subsurface structures around Japan island using waveform tomography with a densely distributed network of permanent seismometers.

Key words: Crustal structure, Crustal imaging, Waveform inversion, Japan

1 INTRODUCTION

The island nation of Japan is located on the convergent boundary where the Philippine Sea plate and the Pacific plate are subducting beneath the Eurasian and the Okhotsk plates.

The interactions of these four plates are responsible for many of Japan's unique tectonic features. The boundary between the Pacific and Eurasian plates on land is the Itoigawa–Shizuoka tectonic line (ISTL), which extends from Itoigawa city in Niigata prefecture to Shizuoka city in Shizuoka prefecture. The subduction of the Philippine Sea Plate created the Izu–Bonin (arc–arc) collision zone (IBCZ), where the Izu–Bonin arc has collided with the Honshu arc. The area also includes two prominent structural features: the Median tectonic line (MTL) and the Niigata–Kobe tectonic line (NKTL).

Central Japan contains many active volcanoes, sedimentary basins, the IBCZ, and several major tectonic lines (ISTL, MTL, and NKTL). Therefore, the seismic structure of the region is expected to contain substantial lateral heterogeneities. The complex geological structures of central Japan have been the subject of many previous geophysical studies, which have relied mainly on regional- and exploration-scale seismic tomography (Arai et al., 2013; Arai & Iwasaki, 2014; J. Nakajima & Hasegawa, 2007a, 2007b; Nishida et al., 2008; Nimiya et al., 2020). For example, a series of studies using first-arrival tomography (J. Nakajima & Hasegawa, 2007a, 2007b; J. Nakajima et al., 2009) revealed the slab geometry of the Philippine Sea Plate and investigated plausible relationships between the arc magmatism and the subducting oceanic plates. Nishida et al. (2008) and Nimiya et al. (2020) leveraged the ambient noise wavefield using seismic interference and clearly imaged underground structures including magmatic fluids and thick sedimentary successions.

Recently, the development of adjoint waveform tomography techniques has improved our ability to resolve subsurface structures (Fichtner et al., 2010; Tape et al., 2010; Simute˙ et al., 2016; Lei et al., 2020). In this method, three-dimensional (3D) sensitivity distributions of seismic waves can be computed by full numerical seismic wave simulation in heterogeneous media using the adjoint method (Fichtner, 2010; Peter et al., 2011). Furthermore, first-arrival tomography and ambient noise tomography use specific seismic phases, whereas adjoint waveform tomography can use as much waveform information as possible without requiring selections of seismic phases. Therefore, the application of adjoint waveform tomography

might improve tomographic imaging of heterogeneous seismic velocity structures beneath central Japan.

The goals of the present work are to resolve crustal S-wave velocity structures in central Japan based on adjoint waveform tomography, and to investigate whether it is possible to obtain detailed tomographic images comparable to those resolved by other popular methods (e.g., first-arrival or ambient noise tomography). Our study differs from previous applications of adjoint waveform tomography in Japan (Miyoshi et al., 2017), in that our target is a larger area and we use many more seismic stations. Here, we apply adjoint waveform tomography to the large volume of seismic data collected by Hi-net (Okada et al., 2004). The estimated crustal S-wave velocity model reaches a minimum misfit after 36 iterations and shows strong lateral velocity variations. The velocity anomalies in the estimated model are in good agreement with the geology.

2 DATA

Earthquake waveform data were collected from the Hi-net high-sensitivity seismograph network, operated across Japan by the National Research Institute for Earth Science and Disaster Prevention (NIED) (Okada et al., 2004). There are 358 Hi-net permanent stations in our study area (Figure 1(a)), all have three-component velocity seismometers and are deployed in boreholes. The seismometers are designed to have sensitivities >1.0 Hz; however, our target frequency range is 0.033–0.125 Hz. Therefore, we applied the sensitivity corrections proposed by Maeda et al. (2011) to use low-frequency seismic waves. We collected data from 70 earthquakes that occurred between 2004 and 2019 with moment magnitudes $4.2 \leq Mw \leq 5.8$ and depths shallower than 60 km (Figure 1(c),(d)). Earthquake parameters for simulations were extracted from their Global CMT solutions (Ekström et al., 2012); these values were fixed while updating our velocity models, because inversion for source parameter updates requires additional computation time. In addition, we restricted the data to recordings at source–receiver distances of >80 km.

3 METHOD

3.1 3D seismic wave simulation and initial model

Synthetic waveforms of 240 sec were calculated using the spectral element method, which is widely used in seismology due to its accuracy and ease of code parallelisation (Komatitsch & Tromp, 1999, 2002; Tape et al., 2010). We used the program SPECFEM3D for forward and adjoint 3D isotropic seismic wave simulations (Peter et al., 2011). We selected Lagrange polynomials of degree 5 to represent the seismic wavefield in our target region.

The laterally homogeneous seismic velocity model named JMA2001 was used as the initial model (Ueno et al., 2002); this provides S- and P- wave velocity structures around Japan. We obtained initial density structures using empirical relationship between P-wave velocity and density (Brocher, 2005):

$$\rho = 1.6612V_p - 0.4721V_p^2 + 0.0671V_p^3 - 0.0043V_p^4 + 0.000106V_p^5, \quad (1)$$

where ρ is in g/cm^3 and V_p is in km/sec.

3.2 Misfit of waveforms

Noisy observed data, which is dissimilar to synthetic data, could result in incorrect model parameters. In addition, cycle skipping can lead to a local minimum in the waveform inversion's solution space that does not correspond to true structure. The latter phenomenon can occur when observed waveforms are more than half a wavelength out of phase from synthetic waveforms; therefore, data selection must be carried out as carefully as possible to prevent this. In this study, we automatically determine the time windows of pairs of synthetic and observed waveforms based on parameters such as time lag, the cross-correlation coefficient between observed and synthetic waveforms, and the signal-to-noise ratio, using the program FLEXWIN (Maggi et al., 2009). We optimized the model parameters in two frequency ranges: 0.0333–0.1 and 0.0333–0.125 Hz. Thus, time-window selection was carried out in the first iteration for each frequency range. As a result, time windows were determined for 22,825 waveform pairs in the 0.033–0.1 Hz range and 28,819 in the 0.033-0.125 Hz range.

The quantification of the misfit between synthetic and observed waveforms was based on phase misfit using the time-frequency transform (Fichtner et al., 2008, 2009).

3.3 Model update

We compute sensitivity kernels with respect to model parameters using the adjoint method (Fichtner, 2010), then use these in a conjugate-gradient optimization with step lengths set so that the change from the previous model was always <6%. We use a multiscale strategy that first recovers the smooth Earth‘s structures, then resolve finer-scale structures by broadening the frequency range (from 0.033–0.1 to 0.033–0.125 Hz). The most energetic phase in our data is the surface wave; therefore, only the S-wave velocity was updated between iterations.

4 RESULTS AND INTERPRETATIONS

After 32 iterations of the 0.033–0.1 Hz band and 4 iterations of the 0.033–0.125 Hz band we obtained the S-wave velocity model shown in Figure 2. The results show strong horizontal velocity variations: for example, at 10 km depth, low-velocity anomalies reach <3000 m/s, whereas high-velocity anomalies are ∼4000 m/s. The misfit is reduced by 18.0% in the 0.033–0.1 Hz band after 32 iterations and 1.6% in the 0.033–0.125 Hz band after 4 iterations (Figure 3). We confirmed that the misfits between observed and synthetic waveforms were improved after 36 iterations; representative examples are shown in figures 4 and 5. In figure 4, panel A shows that the waveforms corresponding to the initial model are faster than the observed waveforms; therefore, the perturbations from the initial model take negative values around the path between the earthquake and seismometer A (figure 4). In contrast, the perturbation values are positive around the paths between the earthquake and other seismometers (B, C, and D, in figure 4). This agrees with the observation that the waveforms corresponding to the initial model in these panels arrive later than the observed waveforms.

The largest feature in the resultant S-wave velocity model is that the northern part of the study area is characterized by low velocities, whereas high velocities dominate in the south. This general finding agrees with previous studies (J. Nakajima & Hasegawa, 2007a; Nishida

et al., 2008). In addition, many earthquakes are distributed at the low-velocity anomalies (figure 2).

At 5 km depth, there is a distinct low-velocity anomaly around region A. The Niigata sedimentary basin, which formed during the opening of the Japan Sea (Takano, 2002), covers a portion of this low-velocity anomaly. As expected, the thick sedimentary rocks of the Niigata basin yield lower seismic velocities. In addition, multiple active volcanoes, such as Asama mountain and Kusatsu–Shirane mountain, are in this region. Therefore, the low-velocity anomaly could be due in part to the sedimentary basin as well as magmatic fluids associated with back-arc volcanism.

The high-velocity anomaly trending from southwest to northeast is located around the region B at all depth images (figures 2). This anomaly may be associated with the granitic rocks in the Ryoke-belt. Cretaceous low-pressure metamorphic belt located along the north side of the MTL (T. Nakajima, 1994). The anomaly coincides with the Ryoke belt in the Chubu area, and with local granitoids emplaced into the metamorphic rocks of the belt (T. Nakajima, 1994; Ishihara & Chappell, 2007). Thus, igneous rocks that are harder than their surrounding rocks may be responsible for the high velocities in region B.

The distributions of velocity anomalies are consistent with the previous velocity model using first-arrival tomography (J. Nakajima & Hasegawa, 2007a). However, for example, the Kanto mountain can be seen clearly as high velocity block at 5–10 km depth in our results (figure 2), and this feature is not present in the velocity model of J. Nakajima and Hasegawa (2007a). This could be derived from the larger number of ray paths of Nakajima and Hasegawa (2007a) or incorporating surface wave of our inversion. In fact, the high velocity block of Kanto mountain is present in the S-wave velocity model derived from ambient noise tomography using surface wave (Nishida et al., 2008). However, the high velocity anomaly around the Ryoke-belt is more clear than Nishida et al. (2008) and we infer that the result of our study has higher lateral resolution than the velocity model derived only from surface wave.

5 DISCUSSION

We conducted a checkerboard test to assess the resolution and reliability of the S-wave velocity model. In this test, cube-shaped anomalies with velocity perturbations of ±18% relative to the background were inserted into the JMA2001 model (figure 6). The area of each anomaly was 35km × 35 km, which is suitable for evaluating the reliability of the high- and low-velocity anomalies resolved in Figure 2. Because our goal was to construct an S-wave velocity model, anomalies were only introduced into S-wave velocity, not P-wave velocity or density. When sensitivity kernels were calculated for the checkerboard test, we used the same time windows for seismogram pairs as those in the model estimation. We then tried to invert the checkerboard model using the JMA2001 model without anomalies.

Figure 6 shows the results of the checkerboard test sliced at 5, 10, 15, and 20 km depths. At 10 and 15 km depths, the checkerboard pattern is clearer than at other depths. Therefore, our data set (earthquakes and stations) and frequency ranges (0.033–0.1 and 0.033–0.125 Hz) seem to be most sensitive to structures at depths of 10–15 km. At 20 km depth, sensitivity is lower than at shallower depths. In addition, we confirmed that the checkerboard pattern could not be resolved at depths below 25 km. Therefore, based on our sensitivity test, we conclude that the S-wave velocity structure in figure 2 is reliable at depths up to 15 km.

We estimated 3D S-wave velocity structure in central Japan by exploiting the advantages of adjoint waveform tomography, such as full numerical calculation of seismic wave propagation, 3D sensitivity distributions of seismic waves, and incorporating as many seismic phases as possible. As discussed in section 4, the resultant S-wave velocity model was consistent with the geology and produced waveforms that fit the observed data (figure 4 and 5). Therefore, the new velocity model will increase the accuracy of earthquake source parameter estimates. Previous study confirmed that using a 3D rather than 1D velocity model improves the estimation of earthquake source parameters, owing to the incorporation of the effects of structural inhomogeneities (Hejrani et al., 2007).

6 CONCLUSIONS

From seismic waveforms from 70 earthquakes recorded by 358 Hi-net seismic stations we built a 3D S-wave velocity model using adjoint waveform tomography. The model estimation procedure was designed to minimize the time-frequency phase misfit between observed and synthetic seismic waveforms in the frequency bands 0.033–0.1 and 0.033–0.125 Hz. We used conjugate-gradient optimization and obtained a final S-wave velocity model after 36 iterations. The final model resolves strong horizontal heterogeneities, with velocity values in the range 2800–4000 m/s. The low-velocity anomalies resolved in the present work appear to correspond to a thick sedimentary basin and volcanic fluids. Granitic rocks of the Ryoke-belt are plausible causes of the high-velocity anomalies. Based on a checkerboard test, our data set and frequency ranges are sensitive to depths of 15 km in the continental region of central Japan. Therefore, we expect that our model has high accuracy for that region. In addition, the improved fit between observed and calculated waveforms obtained with our final model supports the accuracy of the results.This study confirms that adjoint waveform tomography and densely distributed Hi-net stations in Japan can resolve S-wave velocity structure and explain known geology,yielding results comparable to other velocity models and seismic waveforms similar to observed data. Although we have not yet confirmed that earthquake data recorded by Hi-net stations have sufficient resolution for other regions characterized by complex geologic features, such as Kyushu and Hokkaido, the combination of adjoint waveform tomography and Hi-net station data will lead to accurate velocity models throughout the Japanese islands.

7 ACKNOWLEDGMENTS

This work was supported by the Japan Society for the Promotion of Sciencce (JSPS) through a Grant-in-Aid for JSPS Research Fellow (JP21J21871). We used the open-source soft-ware SPECFEM3D for seismic wave simulation and we thank the developers of SPECFEM3D. We also thank the National Research Institute for Earth Science and Disaster Prevention (NIED) for providing us with Hi-net data. Seismic wave simulations were conducted on the

3-D Crustal Shear Wave Velocity Model Derived from the Adjoint Waveform Tomography in the Central

ITO supercomputer system at the Research Institute for Information Technology, Kyushu University. We used the open-source software GMT (Generic Mapping Tools)(Wessel et al., 2013) to construct figures.

8 DATA AVAILABILITY

The Hi-net data is available from https://hinetwww11.bosai.go.jp/auth/?LANG=en. The CMT solutions used in this study are available from https://www.globalcmt.org/. The S-wave velocity model we built is avail-able at https://doi.org/10.6084/m9.figshare.14811255.v1.

REFERENCES

Arai, R., & Iwasaki, T., 2014. Crustal structure in the northwestern part of the izu collision zone in central japan. Earth, Planets and Space 66(1), 1–12.

Arai, R., Iwasaki, T., Sato, H., Abe, S., & Hirata,N., 2013. Crustal structure of the izu collision zone in central japan from seismic refraction data. Journal of Geophysical Research: Solid Earth 118(12), 6258–6268.

Brocher, T. M., 2005. Empirical relations between elastic wave speeds and density in the earth's crust. Bulletin of the seismological Society of America 95(6),2081–2092.

Ekström, G., Nettles, M., & Dziewo ński, A. M., 2012. The global cmt project2004–2010: Centroid-moment tensors for 13,017 earthquakes. Physics of theEarth and Planetary Interiors 200, 1–9.

Fichtner, A., 2010. Full seismic waveform modelling and inversion. Springer Sci-ence & Business Media.

Fichtner, A., Kennett, B. L. N., Igel, H., & Bunge, H. P., 2008. Theoretical background for continental-and global-scale full-waveform inversion in the time–frequency domain. Geophysical Journal International 175(2), 665–685.

Fichtner, A., Kennett, B. L. N., Igel, H., & Bunge, H. P., 2009. Full seismic waveform tomography for upper-mantle structure in the australasian region using adjoint methods. Geophysical Journal International 179(3), 1703–1725

Fichtner, A., Kennett, B. L. N., Igel, H., & Bunge, H. P., 2010. Full waveform tomography for radially anisotropic structure: new insights into present and past states of the australasian upper mantle. Earth and Planetary Science Letters 290(3-4), 270–280.

Hejrani, B., Tkalčić, H., & Fichtner, A., 2007. Centroid moment tensor catalogue using a 3-d continental scale earth model: Application to earthquakes in papuanew guinea and the solomon islands. Journal of Geophysical Research: Solid Earth 122(7), 5517–5543

Ishihara, S., & Chappell, B. W., 2007. Chemical compositions of the late cretaceous ryoke granitoids of the chubu district, central japan–revisited. Bulletinc of the Geological Survey of Japan 58(9/10), 323–350.

Komatitsch, D., & Tromp, J., 1999. Introduction to the spectral element method for three-dimensional seismic wave propagation. Geophysical journal international 139(3), 806–822.

Komatitsch, D., & Tromp, J., 2002. Spectral-element simulations of global seismic wave propagation—i. validation. Geophysical Journal International 149(2),390–412.

Lei, W., Ruan, Y., Bozdağ, E., Peter, D., Lefebvre, M., Komatitsch, D., Tromp, J., Hill, J., Podhorszki, N., & Pugmire, D., 2020. Global adjoint tomography model glad-m25. Geophysical Journal International 223(1), 1–21.

Maeda, T., Obara, K., Furumura, T., & Saito, T., 2011. Interference of long-period seismic wavefield observed by the dense hi-net array in japan. Journal of Geophysical Research: Solid Earth 116(B10)

Maggi, A., Tape, C., Chen, M., Chao, D., & Tromp, J., 2009. An automated time-window selection algorithm for seismic tomography. Geophysical Journal Inter-national 178(1), 257–281

Miyoshi, T., Obayashi, M., Peter, D., Tono, Y., & Tsuboi, S., 2017. Adjoint tomography of the crust and upper mantle structure beneath the kanto region using broadband seismograms. Progress in Earth and Planetary Science 4(1), 1–20.

Nakajima, J., & Hasegawa, A., 2007a. Deep crustal structure along the niigata-kobe tectonic zone, japan: Its origin and segmentation. Earth, planets and space 59(2), e5–e8.

Nakajima, J., & Hasegawa,A., 2007b. Subduction of the philippine sea plate beneath southwestern japan: Slab geometry and its relationship to arc magmatism. Journal of Geophysical Research: Solid Earth 112(B8)

Nakajima, J., Hirose, F., & Hasegawa, A., 2009. Seismotectonics beneath the tokyo metropolitan area, japan: Effect of slab-slab contact and overlap on seismicity. Journal of Geophysical Research: Solid Earth 114(B8).

Nakajima, T., 1994. The ryoke plutonometamorphic belt: crustal section of the cretaceous eurasian continental margin. Lithos 33(1-3), 51–66.

Nimiya, H., Ikeda, T., & Tsuji, T., 2020. Three-dimensional s wave velocity structure of central japan estimated by surface-wave tomography using ambient noise. Journal of Geophysical Research: Solid Earth 125(4), e2019JB019043.

Nishida, K., Kawakatsu, H., & Obara, K., 2008. Three-dimensional crustal s wave velocity structure in japan using microseismic data recorded by hi-net tiltmeters. Journal of Geophysical Research: Solid Earth 113(B10).

Okada, Y., Kasahara, K., Hori, S., Obara, K., Sekiguchi, S., Fujiwara, H., & Yamamoto, A., 2004.

Recent progress of seismic observation networks in japan-hi-net, f-net, k-net and kik-net-. Earth, Planets and Space 56(8), xv–xxviii.

Peter, D., Komatitsch, D., Luo, Y., Martin, R., Goff, N. L., Casarotti, E., Loher, P. L., Magnoni, F., Liu, Q., Blitz, C., Nissen-Meyer, T., Basini, P., & Tromp, J., 2011. Forward and adjoint simulations of seismic wave propagation on fully unstructured hexahedral meshes. Geophysical Journal International 186(2), 721–739.

Simutė, S., Steptoe, H., Cobden, L., Gokhberg, A., & Fichtner, A., 2016. Full-waveform inversion of the japanese islands region. Journal of Geophysical Research: Solid Earth 121(5),3722-3741.

Takano, O., 2002. Changes in depositional systems and sequences in response to basin evolution in a rifted and inverted basin: an example from the neogeneniigata-shin'etsu basin, northern fossa magna, central japan. Sedimentary Geology 152(1-2), 79–97.

Tape, C., Liu, Q., Maggi, A., & Tromp, J., 2010. Seismic tomography of the southern california crust based on spectral-element and adjoint methods. Geophysical Journal International 180(1), 433–462

Ueno, H., Hatakeyama, S., Aketagawa, T., Funasaki, J., & Hamada, N., 2002. Improvement of hypocenter determination procedures in the japan meteorological agency (in japanese). Q. J. Seismol 65, 123–134.

Wessel, P., Smith, W., Scharroo, R., Luis, J., & Wobbe, F., 2013. Generic mapping tools: improved version released. Eos, Transactions American Geophysical Union 94(45), 409–410.

Yano, T. E., Takeda, T., Matsubara, M., & Shiomi, K., 2017. Japan unified high-resolution relocated catalog for earthquakes (juice): crustal seismicity beneath the Japanese Islands. Tectonophysics 702, 19–28.

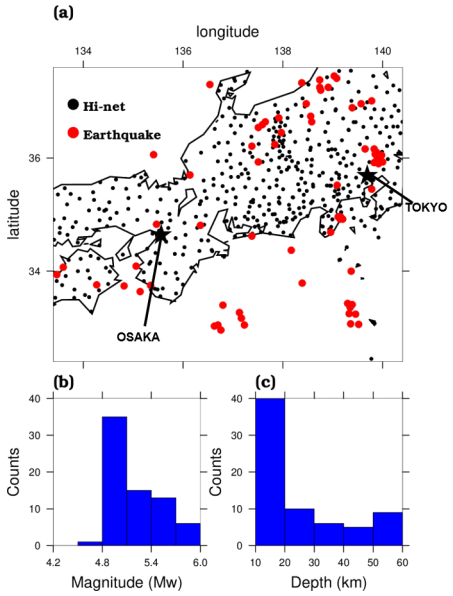

Figure 1. (a)The distributions of seismometers of Hi-net and earthquakes. (b)The magnitude of earthquakes used in this study. (c)The depths of earthquake used in this study.

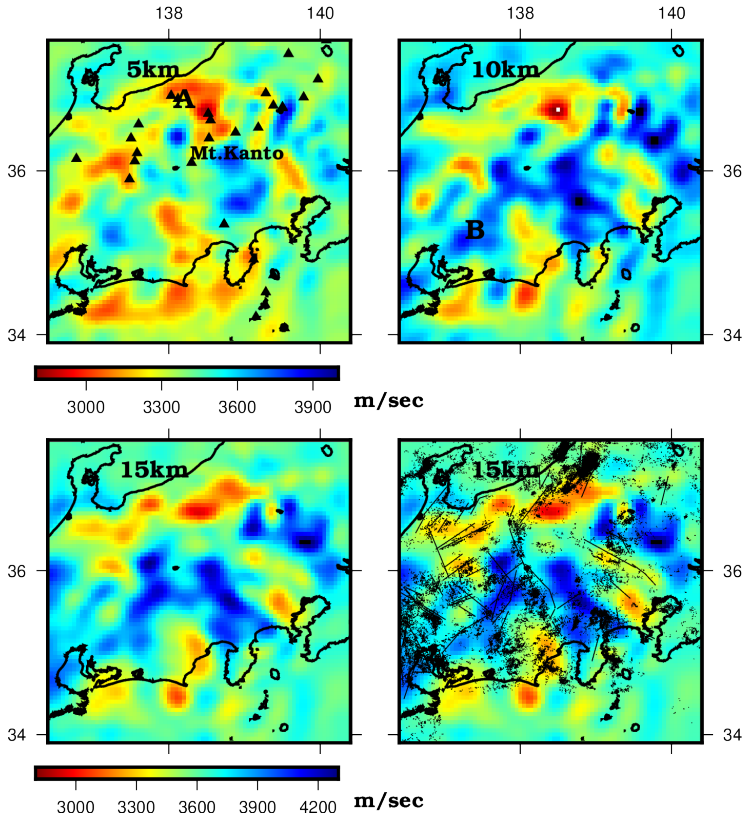

Figure 2. Horizontal slices of the S-wave tomographic model at depths of 5, 10, and 15 km. The bottom-right figure shows the S-wave tomographic model at depth of 15 km with the distributions of faults and earthquakes. We used JUICE catalog (Yano et al., 2017) for the lcoations of hypocenters. We plotted hypocenters located between 10 and 20 km depth. Black triangles denote volcanoes.

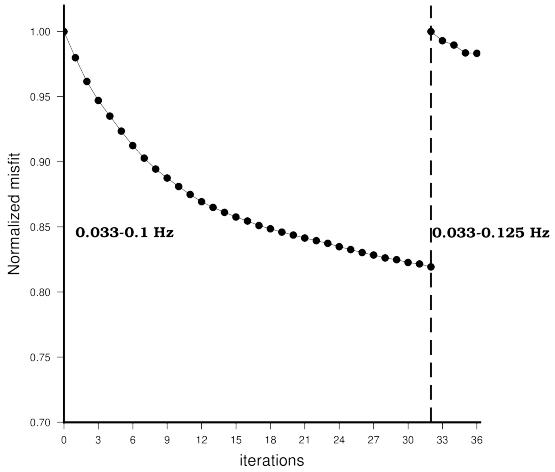

Figure 3. Normalized misfit reductions in the frequency ranges 0.033–0.1 and 0.033–0.125 Hz, respectively.

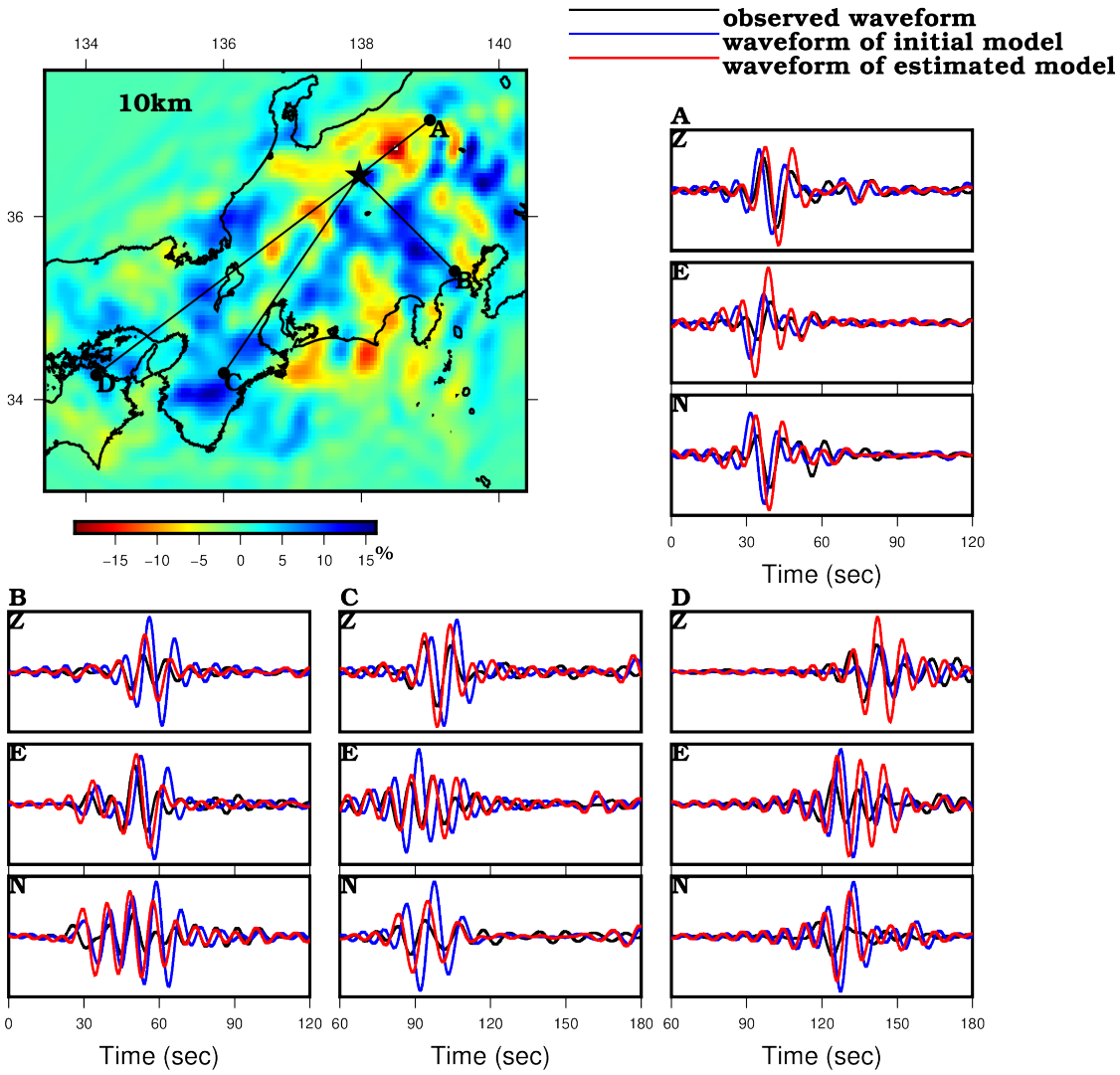

Figure 4. The improvement of waveform fittings. The upper-left subfigure shows velocity perturbations from the initial model at 10 km depth. The black star and circles indicate the epicenters and seismometers, respectively. Panels A–D show observed waveforms (black lines), waveforms of the initial model (blue lines), and waveforms of the final model (red lines), corresponding to the seismometers in the top-left figure. In each panel, vertical (Z), eastward (E), and northward (N) components are shown.

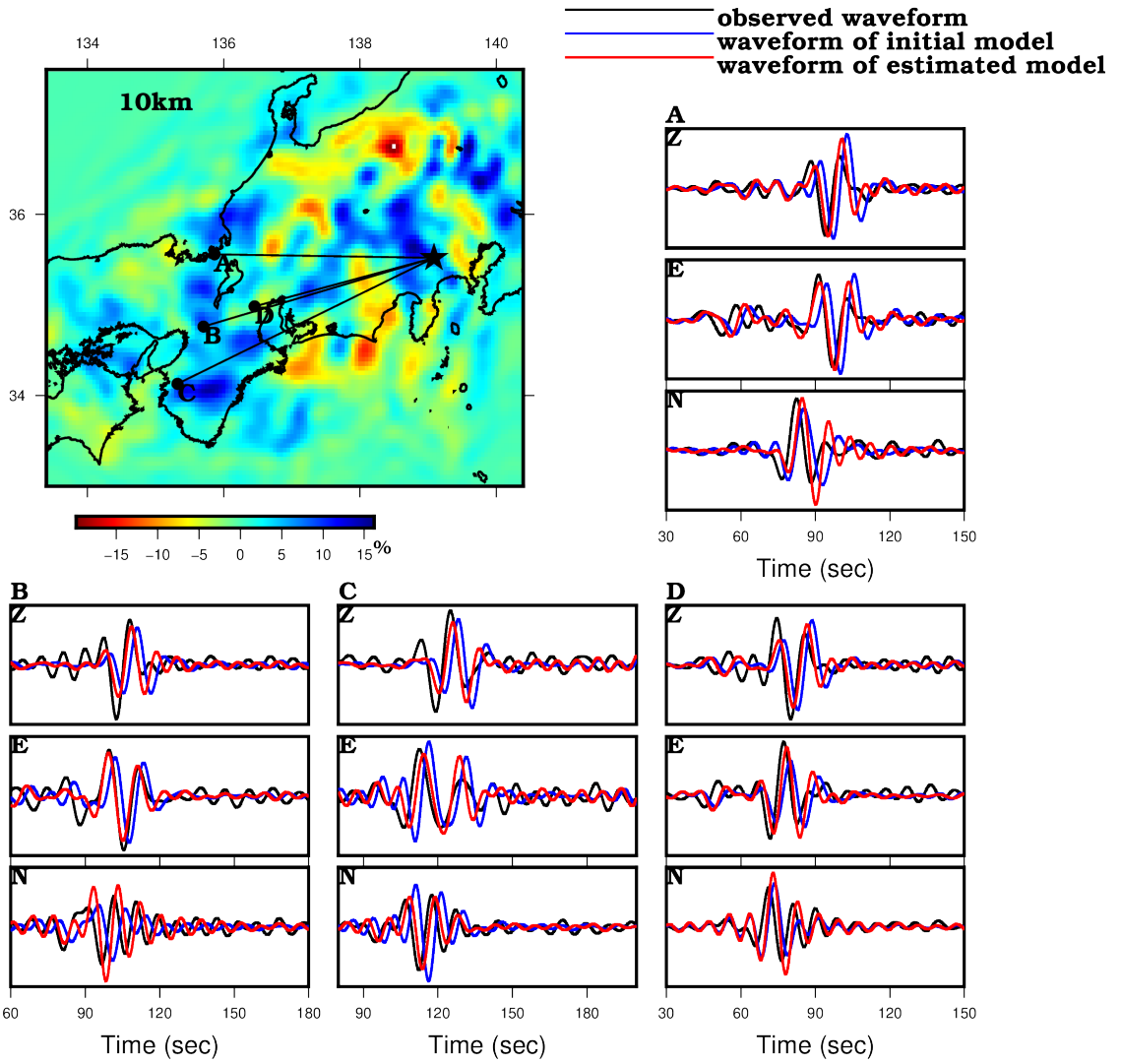

Figure 5. This figure is the same as figure 4 but shows the results of different earthquake-station pairs. The upper-left subfigure shows the velocity perturbation from the initial model at 10 km depth. The black star and circles indicate the epicenters and stations, respectively. Panels A–D show observed waveforms (black lines), waveforms of the initial model (blue lines), and waveforms of the final model (red lines), corresponding to seismometers in the top-left figure. In each panel, vertical (Z), eastward (E), and northward (N) components are shown.

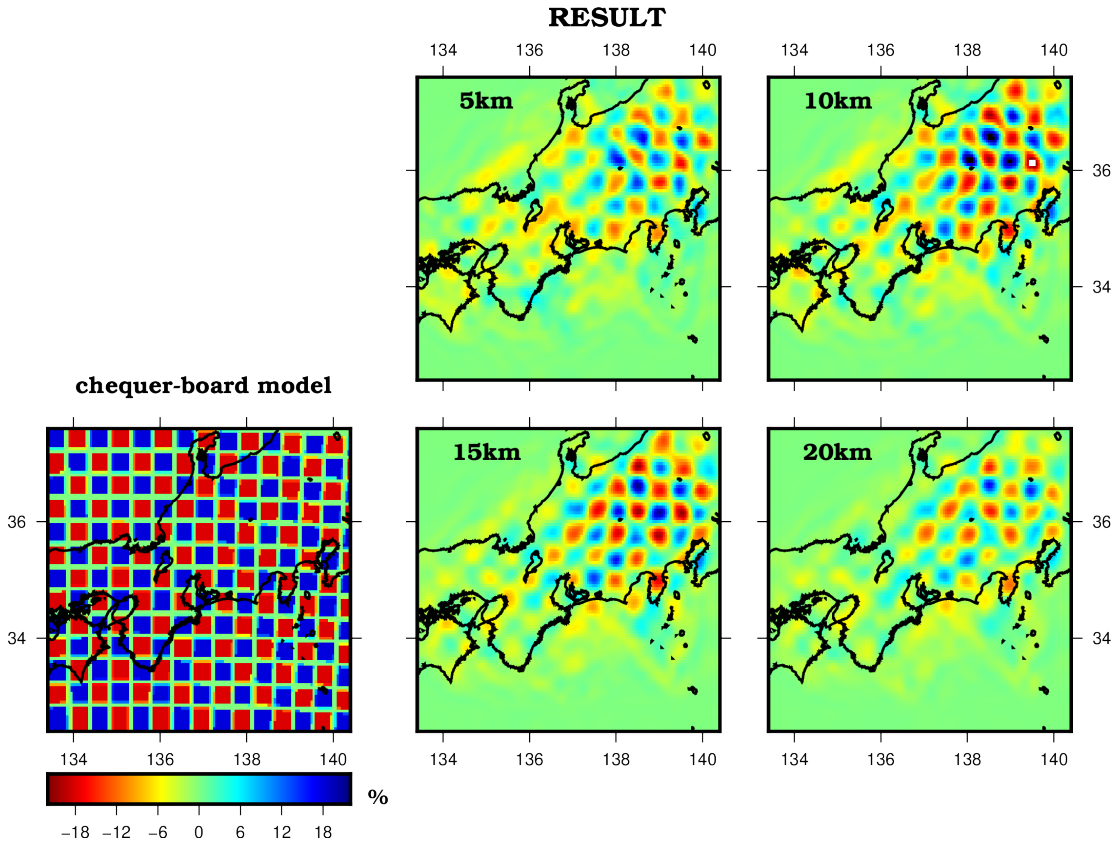

Figure 6. Checkerboard test. The left subfigure shows the checkerboard model used in the resolution test. The remaining four subfigures show the results of the checkerboard test at depth slices of 5, 10, 15, and 20 km, respectively.